Research Article

INTERNATIONAL JOURNAL OF ADVANCED ROBOTIC SYSTEMS

International Journal of Advanced Robotic Systems
November-December 2018: 1–19

DOI: 10.1177/1729881418817634
journals.sagepub.com/home/arx
SAGE

A new novel six-degree of freedom two-link manipulator using active magnetic bearing: Design, kinematics, and control

Mohamed Selmy[1], Mohamed Fanni[1], Abdelfatah M Mohamed[1] and Tomoyuki Miyashita[2]

Abstract

Due to the absence of mechanical contact, active magnetic bearing can be electrically controlled in an accuracy of a micrometer. This makes it a good choice to be used for robot manipulation in the micrometer scale, especially in environments that need to be very clean, for example, surgery or clean rooms. Moreover, it can be used in the applications that need high precision micromotion such as semiconductor wafers manipulation. Despite all these benefits, there are few studies that have investigated the application of active magnetic bearing in the robotics field in spotless environments for micromotion applications. This article proposes a new novel six-degree of freedom two-link manipulator using two contactless joints with active magnetic bearing. The key design aspects of the proposed manipulator are presented. The proposed manipulator is designed using finite element method. Each joint roll angle is controlled using a PID-based feedback linearization controller, while a state feedback controller with integral term is used for controlling the active magnetic bearing five-degree of freedom. The stability analysis of the system, under the proposed controller, is carried out. The robustness of the controllers is tested against end effector payload variations. The results demonstrate that the proposed two-link manipulator is feasible and valid for the applications in spotless environments that need high precision accuracy micromotion control. These significant findings have indicated the feasibility of implementing this proposed manipulator in practice and open the door for developing other types of robots with complete contactless joints using active magnetic bearing.

Keywords

Active magnetic bearing, brushless DC motor, finite element method, stability

Date received: 3 August 2018; accepted: 14 November 2018

Topic: Robot Manipulation and Control
Topic Editor: Andrey V Savkin
Associate Editor: Bin He

Introduction

Active magnetic bearing (AMB) uses electromagnetic forces to levitate an object, typically a rotor without friction. It controls the rotor position with an accuracy of a micrometer.[1] AMB possess several remarkable advantages compared to conventional bearing such as lubrication-free operation, extended life, controllable bearing dynamic properties, and frictionless operation.[2] Thus, AMB is used

[1] School of Creative Science and Engineering, Egypt-Japan University of Science and Technology, Alexandria, Egypt
[2] Graduate School of Creative Science and Engineering, Faculty of Science and Engineering, Waseda University, Tokyo, Japan

Corresponding author:
Mohamed Selmy, School of Creative Science and Engineering, Egypt-Japan University of Science and Technology, 21934 Alexandria, Egypt.
Email: mohamed.selmy@ejust.edu.eg

in many industrial applications such as high-speed rotating equipment, machine tool, machining spindle, vacuum pumps or compressors, bearingless motors, artificial heart pumps and flywheel-based energy-storage devices.[3–5]

Due to the absence of friction and lubrication, AMB can be used in spotless environments like clean rooms, surgery rooms, or vacuum chambers. Robots in these environments must be free of any dust or oil generation sources. Therefore, AMB is preferable to be used for the joints of that kind of robots. Tasks in these environments such as silicon wafers transfer for the electronic manufacturing need to move the manipulator end effector with high precision positioning control.

For the past decades, an apparent clear trend in using AMB in robotics could be noticed. In Higuchi et al.,[1] an experimental study of using AMB in robot joints has been made. A prototype of clean room parallel robot consists of two-degree of freedom (2-DOF) and five joints was constructed. However, this study does not lead to a completely contactless joints robot. In Tezuka et al., [6] a novel magnetically levitated motor consists of a five controlled DOFs was investigated theoretically using AMB. A novel contactless 6-DOF active robotic joint using AMB is presented in Selmy et al.[7] and developed in Selmy et al.[8]

Some research has been done to investigate the use of robots in a clean environment for high positioning accuracy applications. For instance, a clean compatible PA10-6C/7C robotic arm is used for semiconductor wafer handling with milli-scale positioning accuracy.[9] However, their joints do not have a magnetic bearing. Koichi Matsuda and Shinya Kijimoto[10] treat a disturbance cancellation problem for minimizing the effects of reaction forces on position accuracy of a clean room robot applied with magnetic bearings. However, the developed robot moves with only 3-DOF to transfer a wafer among processing chambers.

A new design of a force-controlled end effector for robotic polishing tasks is presented in Mohammad et al.[11] The end effector has a polishing head with a linear coil actuator to provide tool compliance using thrust bearing. However, the polishing head of the end effector is driven by geared AC motor and the bearing is of contact type. Other studies of controlling robot arm movement in one-axis direction and mobile robot arm position control are investigated in the study by Božek et al.,[12] Turygin et al.[13], and Lozhkin et al.[14]

In a previous work, a 6-DOF robotic joint with AMB was designed in the study by Selmy et al.[7] Despite the good performance of that joint, it suffers from limited workspace of the end effector movement. Thus, to overcome these limitations, a new two-link manipulator with two novel contactless 6-DOF joints is proposed and developed in this article. This system opens new applications area for AMB in robotics, for example, robots used in clean environments such as clean and surgery rooms, self-reconfiguration robots, robots with selective compliance, industrial robots for laser cutting or arc welding, and space robots.

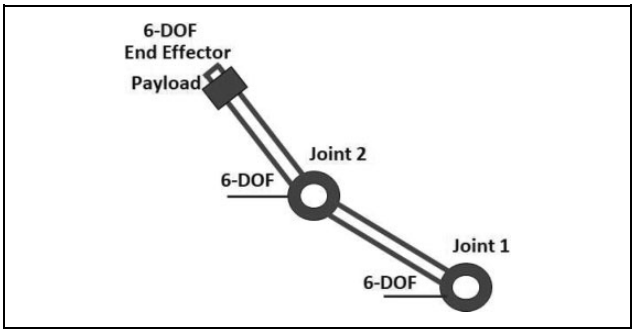

Figure 1. System schematic diagram.

The main contributions of this article are as follow:

(i) A new novel two-link manipulator, which utilizes two novel contactless 6-DOF joints is designed.
(ii) A controller design to track the desired end effector 6-DOF trajectory for micromotion, with precise stability analysis, is carried out.

The rest of this article is organized as follows. In section "Description and design of the proposed system," the description and design of the proposed system are presented. The mathematical model including the dynamics of the motor and AMB for each joint are derived and discussed in section "System dynamic model". The forward and inverse kinematics analysis of the novel system is analyzed in details in section "Kinematics". Proper design of the controllers for each joint is developed and stability analysis of the controller is carried out in section "Control design". In section "Simulation study", the performance of the proposed manipulator is evaluated and its effectiveness in micromotion scale applications is demonstrated. Finally, the conclusions are presented in section "Conclusion".

Description and design of the proposed system

In this section, the two-link manipulator with the two contactless active joints using AMB is described and designed in detail.

System description

A schematic diagram of the proposed system is shown in Figure 1. This system consists of two contactless 6-DOF joints, each one has a frameless brushless DC (BLDC) motor, two radial AMB, one axial AMB, a sensor for measuring the motor shaft roll angle, position sensors to measure the AMBs air gap deviations and the controllers.

The two-link manipulator system block diagram is shown in Figure 2. The actual end effector position and orientation are computed using the data from each of the two contactless joints motor roll angles sensors and the AMB air gap deviations measurement sensors. The controllers minimize the errors between these obtained

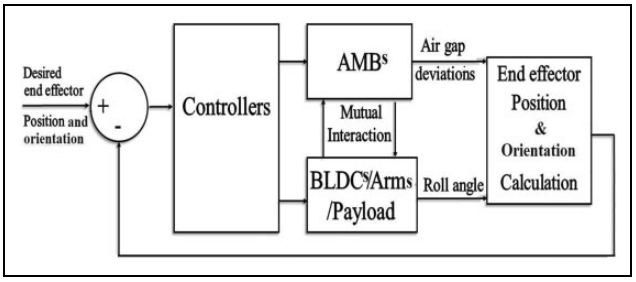

Figure 2. System block diagram.

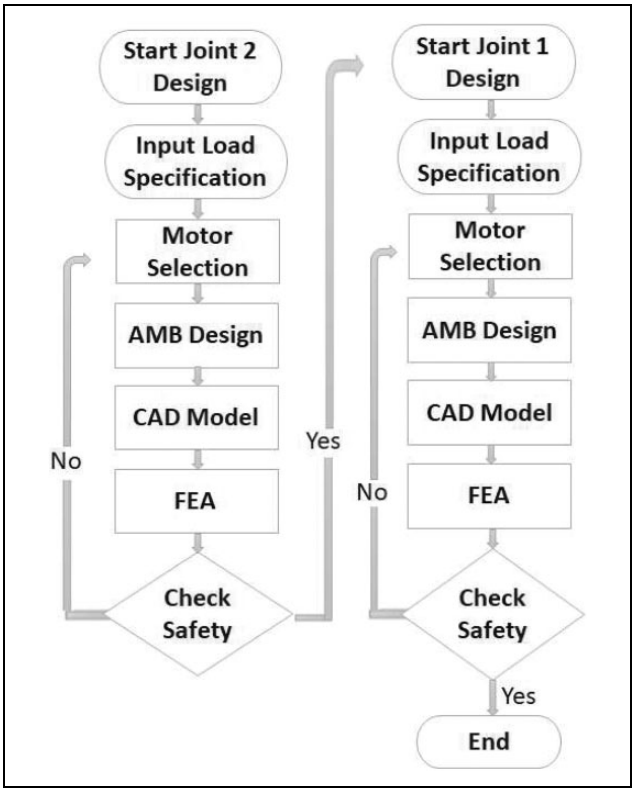

Figure 3. Design process flowchart.

measurements and the desired ones by sending the suitable control signals to the electromagnetic coils of AMB and motors stators windings of each joint. This makes the AMB actuating magnets produce suitable electromagnetic forces and the motors produce suitable torques to maintain the end effector at its desired position and orientation.

System design

Figure 3 shows the design process flowchart of the proposed system. First, the closest joint to the end effector, joint 2, is considered in the design process, then the other joint, joint 1, is designed.

Load torque calculation. Considering the manipulator end effector will pick a payload $m_p = 0.1$ Kg average mass attached to an arm with $250 \times 70 \times 10$ mm^3 dimension, $m_a = 1.15$ Kg mass, and 0.125 m C.G. Location. Figure 4

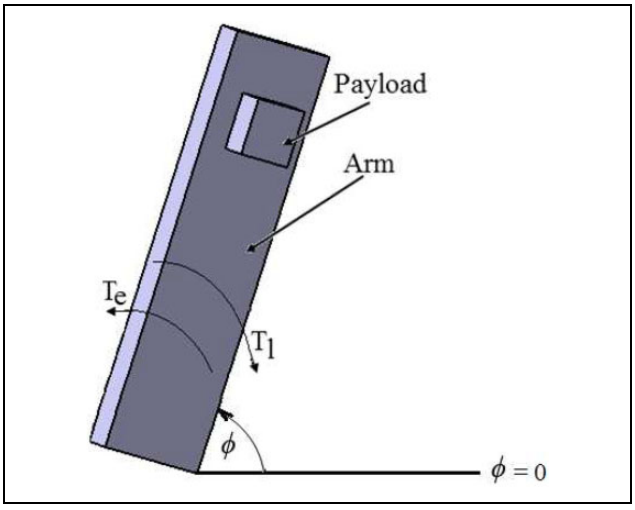

Figure 4. Joint 2 load (arm and payload).

shows the load including arm and payload. This arm will be attach to the motor shaft.

The maximum load Torque, $T_{L2\max}$ is calculated from the following equation

$$T_{L2\max} = (0.195\, m_p + 0.090\, m_a)\, g \tag{1}$$

As a result, the maximum load torque equals 1.2 Nm.

Selection of motor. According to the previous mentioned calculated load torque, a frameless brushless direct drive, 145STK 1M, Alxion BLDC motor[15] is selected. Motor main features are continuous torque of 8 Nm, a speed of 1500 r/min, rotor diameter of 56 mm, and rotor length of 59 mm. According to the rotor diameter and rotor length, the shaft length is calculated and found to be = 310 mm.

AMB electromechanical design. In order to facilitate the design of the electromagnetic coils of the radial AMBs, the total weight to be carried by the two radial AMBs of joint 2 is calculated and it is found to be 5 Kg. Then, the total force carried by the two radial bearings with 20% factor of safety is 58.8 N.

Considering one of the two radial AMBs (the left radial AMB), then the upper electromagnetic force f_{l1} should compensate the lower force f_{l2} in addition to the half of the total weight force at this bearing, then

$$f_{l1} = f_{l2} + \frac{58.8}{2} \tag{2}$$

$$f_j = K\left(\frac{i_j}{D_o + g_j}\right)^2 \left(1 + \frac{2(D_o + g_j)}{\pi h}\right) \tag{3}$$

Using equation (2) for $f_{l2} = 4.6$ N, then $f_{l1} = 34$. Moreover, if the nominal air gap length $D_o = 1$ mm N, air gap variation $g_j = 0$, pole width $h = 40$ mm, and the constant $K = 6.9269\, e^{-05}$ then in equation (3), the electromagnetic

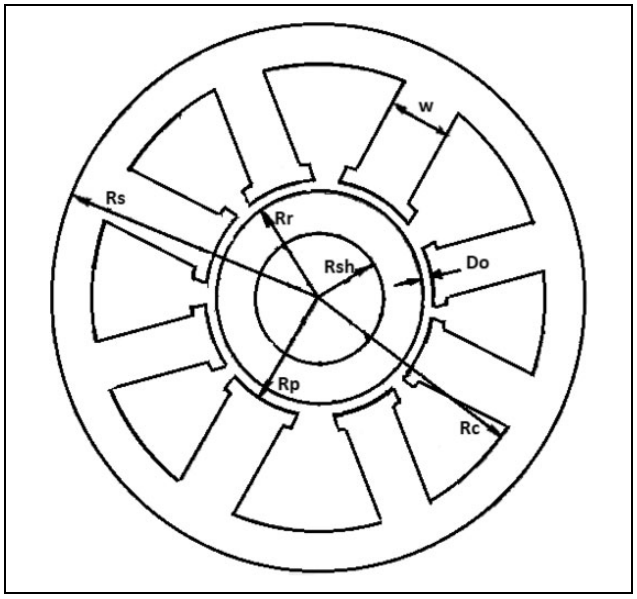

Figure 5. Conventional eight-pole radial AMB. AMB: active magnetic bearing.

coils currents at steady state are $I_{l1} = 0.7006$ A and $I_{l2} = 0.2577$ A, where l_1 and l_2 refer to the upper left and lower left directions, respectively.

A conventional eight-pole radial AMB which has the geometry shown in Figure 5 is chosen.The radial AMB design is developed to find the dimensions of the magnetic actuator based on the maximum load capacity, a number of poles and air gap length.[16]

The flowchart in Figure 6 illustrates the design procedure of each eight-pole radial AMB. First, specify the maximum bearing force, rotor radius, the bearing number of poles, pole angle and the air gap length as an initial step. Then, the design procedure is followed and equations (4) to (12) are used to obtain the dimensions of each of the radial magnetic actuator[16]

$$NI = \frac{2D_o B_{\text{sat}}}{\mu_o} \tag{4}$$

$$N = \frac{NI}{I_{\max}} \tag{5}$$

$$A_c = \frac{NI}{JP_f} \tag{6}$$

$$R_r = \frac{R_{\text{sh}} + D_o \sin\left(\frac{\theta_p}{2}\right)}{1 - 2\gamma \sin\left(\frac{\theta_p}{2}\right)} \tag{7}$$

$$A_g = \frac{2\mu_o F_{\max}}{\frac{1}{2} B_{\text{sat}}^2 n_p \cos(\theta_p)} \tag{8}$$

$$w = 2(R_r + D_o) \sin\left(\frac{\theta_p}{2}\right) \tag{9}$$

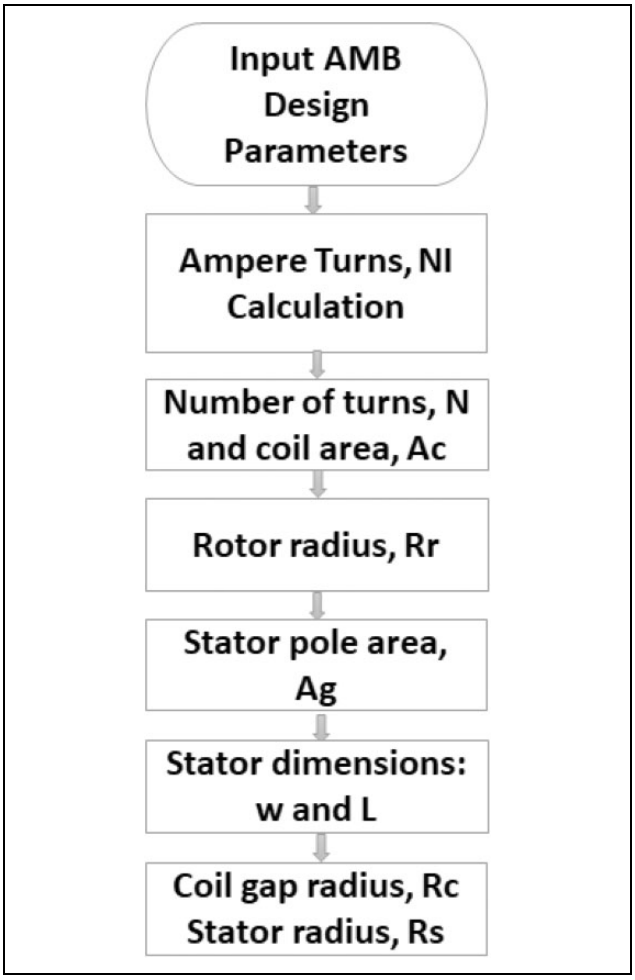

Figure 6. Design procedure of eight pole radial AMB. AMB: active magnetic bearing.

$$L = \frac{A_g}{w} \tag{10}$$

$$R_c = \frac{A_c}{(R_r + D_o)\tan(\theta_p) - \frac{w}{2}} + R_r + D_o \tag{11}$$

$$R_s = R_c + w \tag{12}$$

where B_{sat}, μ_o, $I_{\max}$, $F_{\max}$, J, P_f, R_{sh}, θ_p, γ, and n_p are saturation magnetic flux density, permeability of free space, maximum current, maximum force, wire thermal limit, packing factor, shaft radius, pole angle, flux splitting factor, and magnetic bearing number of poles, respectively.

Table 1 shows the magnetic actuator parameters and the calculated radial AMB dimensions based on the total weight, the dimension of the shaft, and the actuator geometry.

In order to meet the required thrust in the axial direction of joint 2, an axial AMB is designed as shown in Figure 7. The axial AMB consists of the housing parts wound by coils, the disk part located between both of the housing parts. The magnetic thrust force can be expressed by following equation[17,18]

Table 1. Joint 2 radial AMB dimensions.

Design parameter	Value
Maximum force, F_{max2}	30 N
Maximum current, I_{max2}	2 A
Shaft radius, R_{sh2}	21 mm
Saturation magnetic flux density, B_{sat}	1.2 T
Magnetic bearing number of poles, n_{p2}	8
Pole angle, θ_{p2}	22.5°
Wire thermal limit, J_2	4–6 A/mm^2
Flux splitting factor, γ	1
Packing factor, P_f	0.5
Winding number of turns, N_2	950 Turn
Pole Gap Area$_2$, A_{g2}	18 × 40 mm^2
Rotor radius, R_{r2}	35 mm
Stator radius, R_{s2}	125 mm

AMB: active magnetic bearing.

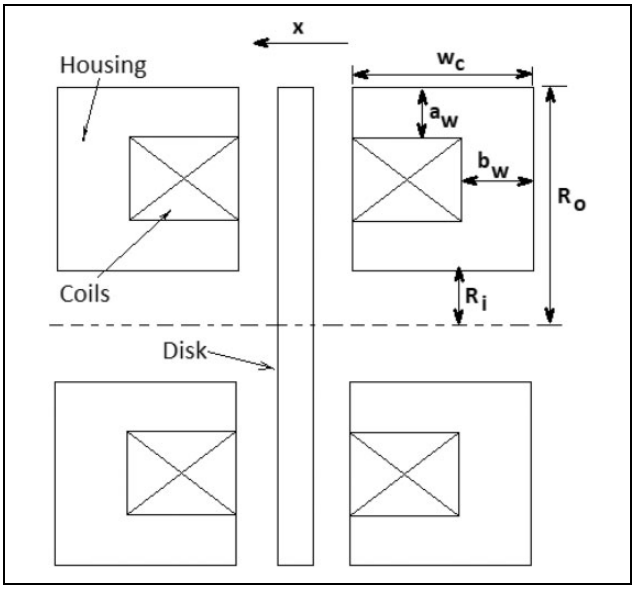

Figure 7. Axial AMB structure. AMB: active magnetic bearing.

$$F_a = \mu_o \left(\frac{Ni}{2x}\right)^2 S \tag{13}$$

where S is the flux area in the air gap, R_o is the outer radius, R_i is the inner radius, $a_w = b_w$ is the core's thickness, and w_c is the housing's width. Table 2 shows the dimension results of the axial AMB.

The same previous steps (from "Load torque calculation", "Selection of motor", and "AMB electromechanical design" sections) of designing the radial and axial AMBs of joint 2 are repeated for joint 1 design. The load of joint 1 is the joint arm as well as the total weight of joint 2 including the BLDC motor, radial AMB, axial AMB, Sensors, arm, payload, and the joint casing. Therefore, The maximum load torque, $T_{L1\,max}$ is calculated and its value is 57 Nm. The suitable frameless brushless motor for this load is 145STK 6M motor.[15] The total weight (weight of joint 2 and joint 1) to be carried by the two radial AMBs of joint 1 is then calculated and found to be 39.8 Kg. Then, the total force carried by the two radial bearings with 20% factor of safety is 469 N. The steady-state electromagnetic coils currents is then computed and found to be $I_{l1} = 1.858$ A and $I_{l2} = 0.2577$ A. Also, the axial AMB is designed to meet the required thrust in the axial direction and its dimensions are calculated. Tables 3 and 4 show the calculated dimensions of the radial and axial AMBs of joint 1, respectively.

Table 2. Joint 2 axial AMB dimensions.

Design parameter	Value
Outer radius, R_{o2}	35 mm
Inner radius, R_{i2}	22 mm
Core's thickness, $a_{w2} = b_{w2}$	2 mm
Housing's width, w_{c2}	8 mm
Axial force, F_{a2}	60 N
Winding number of turns, N_2	270 Turn
Axial current, I_{a2}	1 A

AMB: active magnetic bearing.

Table 3. Joint 1 radial AMB dimensions.

Design parameter	Value
Maximum force, F_{max1}	235 N
Maximum current, I_{max1}	4 A
Shaft radius, R_{sh1}	23 mm
Saturation magnetic flux density, B_{sat}	1.2 T
Magnetic bearing number of poles, n_{p1}	8
Pole angle, θ_{p1}	22.5°
Wire thermal limit, J_1	4–6 A/mm^2
Flux splitting factor, γ	1
packing factor, P_f	0.5
Winding number of turns, N_1	480 Turn
Pole Gap Area$_2$, A_{g1}	15 × 40 mm^2
Rotor radius, R_{r1}	38 mm
Stator radius, R_{s1}	128 mm

AMB: active magnetic bearing.

System CAD model. The system is drawn using CATIA.[19] Figure 8 shows the CAD model of joint 2 while Figure 9 shows joint 2 CAD model details. Figure 10 shows the CAD model of the all system and Figure 11 shows the details of joint 1. In this system, the robot arms with the payloads as well as the rotating parts of the axial magnetic bearing and the roll angle sensors are fixed to the shafts using set screws.

System finite element analysis. The stress and deflection of the system are studied using finite element method, and the results will be illustrated in "Simulation study" section.

Checking system safety. In this step, calculated stress and deflection values are compared with the maximum allowable stress of steel and the length of the air gap.

Table 4. Joint 1 axial AMB dimensions.

Design parameter	Value
Outer radius, R_{o1}	38 mm
Inner radius, R_{i1}	24 mm
Core's thickness, $a_{w1} = b_{w1}$	4 mm
Housing's width, w_{c1}	12 mm
Axial force, F_{a1}	470 N
Winding number of turns, N_1	175 Turn
Axial current, I_{a1}	2 A

AMB: active magnetic bearing.

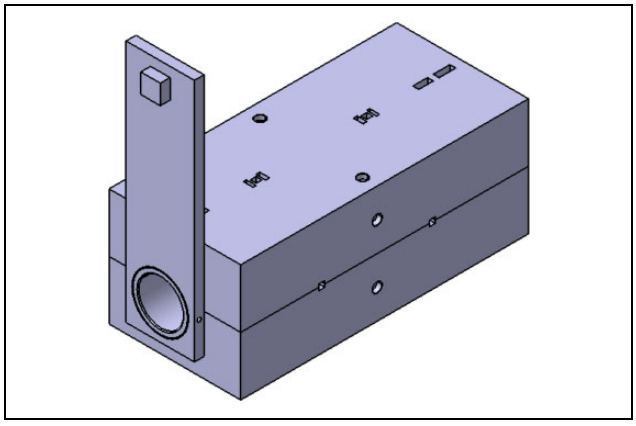

Figure 8. Architecture of joint 2.

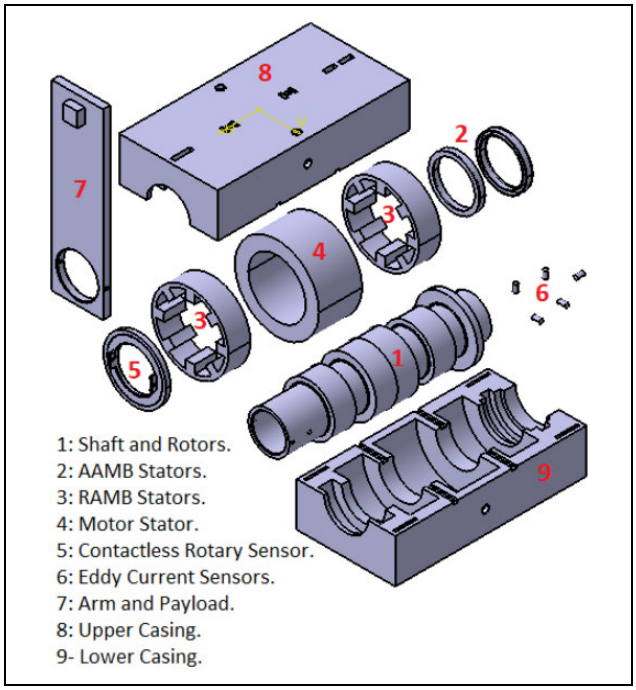

Figure 9. CAD details of joint 2.

System dynamic model

In this section, a multiple-input multiple-output (MIMO) mathematical model of each joint of the system is developed including detailed models for the BLDC motor and the radial and axial AMBs. Moreover, the model of AMB is linearized around the equilibrium point.

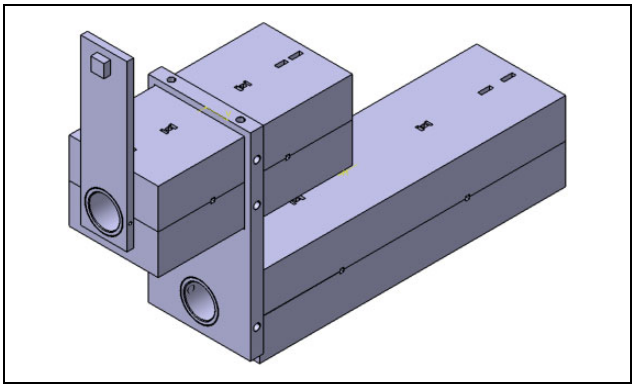

Figure 10. Architecture of the all system.

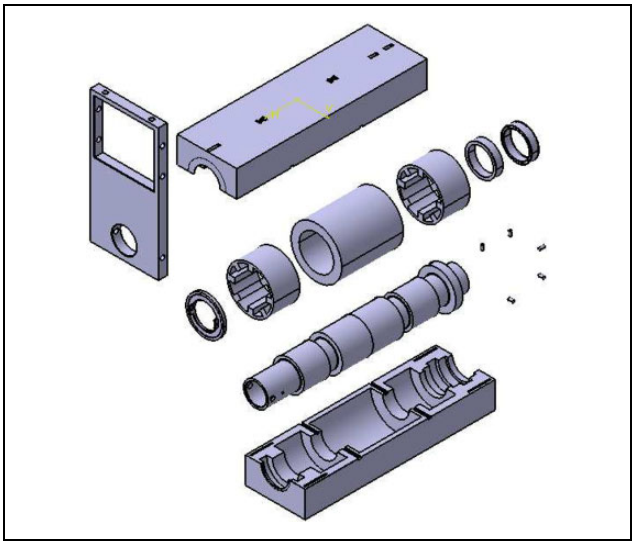

Figure 11. CAD details of joint 1.

BLDC motor dynamic model

Frameless brushless direct drive DC motor is used in this system. This type of motors has the advantages of having no contact part, no gearbox, and compatibility with AMB. The stator windings equations in terms of motor electrical constants for three-phase, star-connected BLDC motor[20] are

$$\begin{bmatrix} v_a \\ v_b \\ v_c \end{bmatrix} = \begin{bmatrix} R & 0 & 0 \\ 0 & R & 0 \\ 0 & 0 & R \end{bmatrix} \begin{bmatrix} i_a \\ i_b \\ i_c \end{bmatrix} + \mathbf{L} \frac{\mathrm{d}}{\mathrm{d}t} \begin{bmatrix} i_a \\ i_b \\ i_c \end{bmatrix} + \begin{bmatrix} e_a \\ e_b \\ e_c \end{bmatrix} \tag{14}$$

$$\mathbf{L} = \begin{bmatrix} L_s - L_m & 0 & 0 \\ 0 & L_s - L_m & 0 \\ 0 & 0 & L_s - L_m \end{bmatrix} \tag{15}$$

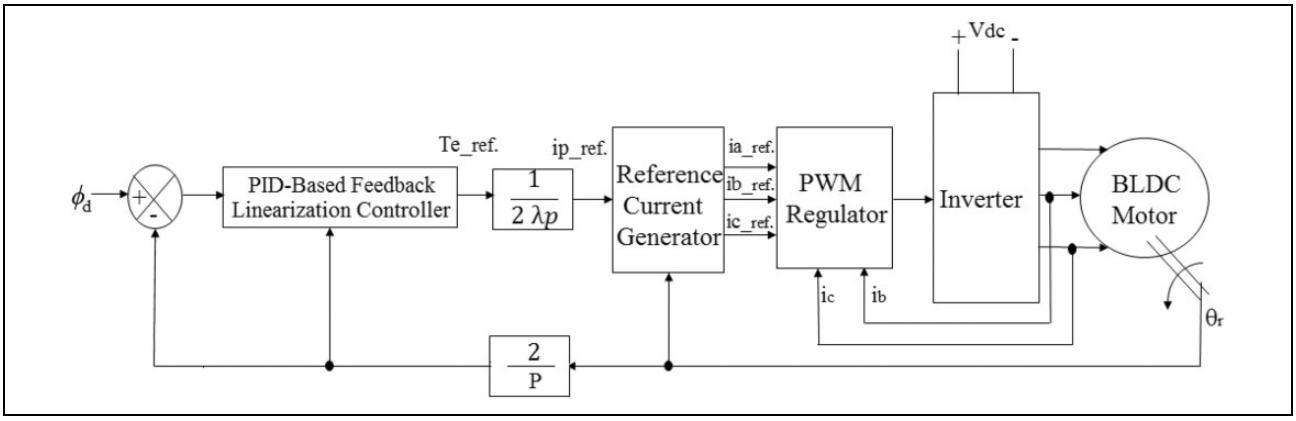

Figure 12. BLDC motor model block diagram. BLDC: brushless DC.

$$T_e = \frac{e_a i_a + e_b i_b + e_c i_c}{\omega_m} \tag{16}$$

$$e_a = f_a(\theta_r)\lambda_p\omega_m, \quad e_b = f_b(\theta_r)\lambda_p\omega_m, \quad e_c = f_c(\theta_r)\lambda_p\omega_m \tag{17}$$

$$\lambda_p = K_p\frac{P}{2} \tag{18}$$

$$T_e - T_l = J_m\frac{\mathrm{d}\omega_m}{\mathrm{d}t} + b_f\omega_m \tag{19}$$

$$T_l = ML_a^2\frac{\mathrm{d}\ddot{\phi}}{\mathrm{d}t^2} + MgL_a\cos(\phi) \tag{20}$$

$$\omega_m = \frac{\mathrm{d}\phi}{\mathrm{d}t} = \frac{2}{P}\omega_r = \frac{2}{P}\frac{\mathrm{d}\theta_r}{\mathrm{d}t} \tag{21}$$

where L_s and L_m are the self inductance and mutual inductance per phase, respectively, and they are assumed to be equal for all phases. The functions $f_a(\theta_r)$, $f_b(\theta_r)$, and $f_c(\theta_r)$ have the same shape as e_a, e_b, and e_c with a maximum magnitude of ± 1. b_f is the motor friction coefficient, J_m is the motor shaft inertia, M is the arm and its payload equivalent mass, T_l is the load electromagnetic torque, λ_p is the motor induced electromotive force (EMF) voltage constant, ϕ is the mechanical roll angle (the rotor angle about X axis).

Figure 12 shows the block diagram of the BLDC motor control system. The joint roll angle is measured and compared with that of the desired trajectory ϕ_d. The roll angle error is controlled through the proportional–integral–derivative (PID)-based feedback linearization controller to provide the required reference torque $T_{e-\mathrm{ref}}$. The stator three-phase reference currents are calculated using equation (16) for a value of torque equals the reference torque. Besides, it is compared with their respective actual values. The three-phase currents errors are controlled using a P controller and a pulse width modulation is used to generate the suitable switching signals for the inverter semiconductor switches.

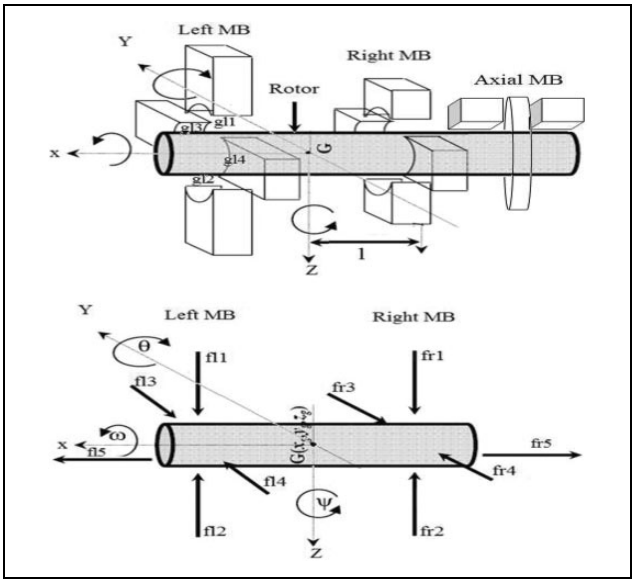

Figure 13. Horizontal shaft AMB diagram. AMB: active magnetic bearing.

AMB dynamic model

Dynamic equations of motion. Figure 13 shows an AMB of horizontal shaft type, it consists of two radial AMBs and one axial AMB. Both of the radial AMBs control the horizontal, vertical, pitch, and yaw motions. The axial AMB controls the axial linear motion. The dynamic equations of this system are given as follows[21,22]

- Axial direction:

linear motion

$$m\ddot{x} = -\beta x - 2\gamma_a\dot{x} + f_{la} - f_{ra} \tag{22}$$

- Radial direction:

Horizontal linear motion

$$m\ddot{y} = f_{l3} - f_{l4} + f_{r3} - f_{r4} - f_{LH} - f_{RH} \tag{23}$$

Vertical linear motion

$$m\ddot{z} = f_{l2} - f_{l1} + f_{r2} - f_{r1} + mg - f_{LV} - f_{RV} \quad (24)$$

Pitching rotational motion

$$J_y\ddot{\theta} = -\omega_r J_x\dot{\psi} + (f_{l1} - f_{l2} + f_{r2} - f_{r1} - f_{LV} - f_{RV})l \quad (25)$$

Yawing rotational motion

$$J_y\ddot{\psi} = \omega_r J_x\dot{\theta} + (f_{l3} - f_{l4} + f_{r4} - f_{r3} - f_{LH} - f_{RH})l \quad (26)$$

- Electromagnetic coil voltage equation

$$e_j = L_C\frac{\mathrm{d}i_j}{\mathrm{d}t} + R_C i_j \quad (27)$$

where $j = l_1 \ldots l_4, r_1 \ldots r_4$.

f_{LV}, f_{RV}, f_{LH}, and f_{RH} are the two radial bearings forces due to the centrifugal force of the robot arm and its payload in the vertical and horizontal directions.

The centrifugal force in the vertical direction is given as follows

$$F_V = ML_a\omega_m^2\sin\phi \quad (28)$$

The centrifugal force in the horizontal direction is given as follows

$$F_H = ML_a\omega_m^2\cos\phi \quad (29)$$

The forces f_{LV}, f_{RV}, f_{LH} and f_{RH} are calculated as follow

$$f_{RH} = \frac{L_1}{L_2}F_H \quad (30)$$

$$f_{LH} = f_{RH} + F_H \quad (31)$$

$$f_{RV} = \frac{L_1}{L_2}F_V \quad (32)$$

$$f_{LV} = f_{RV} + F_V \quad (33)$$

where L_1 is the distance from the robot arm to the left AMB and L_2 is the distance between the two radial AMBs.

- The air gap displacement, g_j is expressed as follow:

$g_j = D_o + g'_j$, where D_o is the air gap length at equilibrium, and g'_j is the air gap deviation which is expressed in terms of y, z, θ and ψ, coordinates of the rotor mass center, as follow

$$\begin{bmatrix} g'_{l1} \\ g'_{r1} \\ g'_{l3} \\ g'_{r3} \end{bmatrix} = -\begin{bmatrix} g'_{l2} \\ g'_{r2} \\ g'_{l4} \\ g'_{r4} \end{bmatrix} = \begin{bmatrix} z - l\theta \\ z + l\theta \\ -y - l\psi \\ -y + l\psi \end{bmatrix} \quad (34)$$

where $g'_{l1}, g'_{l3}, g'_{r1}$, and g'_{r3} represent the air gap deviation at the left AMB in vertical direction, horizontal direction, and right AMB in vertical direction, horizontal direction, respectively. It is obvious that the axial direction linear motion can be controlled separately.

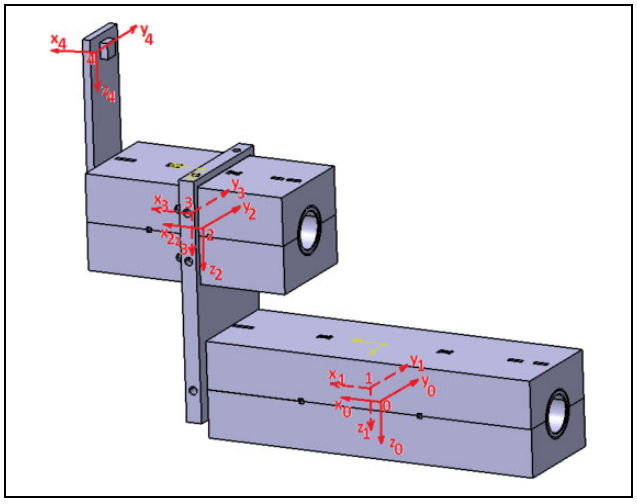

Figure 14. Frames location on the proposed robotic joint.

State variable representation. The state variable representation of radial AMB is given in "Appendix 1: State space representation of AMB." The 4-DOF radial motion is represented by a MIMO nonlinear system with 16 states, 8 inputs (electromagnetic coil voltages), and 4 outputs (air gap deviations). The 1-DOF axial motion is represented by a multi input single output nonlinear system with 4 states, 2 inputs (electromagnetic coil voltages), and 1 outputs (air gap deviation). The 4-DOF system is linearized around the equilibrium point and the following linearized model is obtained, where A_r, B_r, and C_r matrices of the system are given in "Appendix 2: AMB model linearization"[23]

$$\dot{x} = A_r x + B_r u \quad (35)$$

$$y = C_r x \quad (36)$$

In a similar way, the state variable representation and the linearized model for the axial linear motion is obtained and are given in the same previous mentioned appendices.

Kinematics

In Figure 14, the end effector position, and orientation of the two-link manipulator are controlled by controlling the joint angle and the air gap lengths of the AMBs in radial and axial directions of the two contactless joints.

The relation between the end effector position; translation (x_e, y_e, z_e) and rotation $(\phi_e, \theta_e, \psi_e)$ on one hand and the two contactless joints angles and the air gap lengths, on the other hand, is addressed in the following forward and inverse kinematics subsections.

Forward kinematics

The reference frame $f_0(x_0, y_0, z_0)$ is attached to the fixed casing of joint 1, while frame $f_1(x_1, y_1, z_1)$ is attached to the motor shaft of joint 1 and located at half of the distance between the right and left radial AMBs. The two frames, f_0 and f_1, coincide on each other at equilibrium position (zero air gap deviations).

Frame $f_2(x_2, y_2, z_2)$ is attached to the fixed casing of joint 2, while frame $f_3(x_3, y_3, z_3)$ is attached to the motor shaft of joint 2 and both of them are located at half of the distance between the right and left radial AMBs. The two frames, f_2 and f_3, coincide on each other at equilibrium position. Frame $f_4(x_4, y_4, z_4)$ is attached to the end effector.

The relation between frames f_3 and f_4 is determined from the following matrix

$$ {}^3H_4 = \left[\begin{array}{ccc|c} 1 & 0 & 0 & {}^3x_4 \\ 0 & 1 & 0 & {}^3y_4 \\ 0 & 0 & 1 & {}^3z_4 \\ \hline 0 & 0 & 0 & 1 \end{array}\right] \tag{37} $$

where ${}^3x_4$, ${}^3y_4$, and ${}^3z_4$ are constants lengths.

The relation between frames f_2 and f_3 is determined as follows:

Knowing the air gap deviations of the radial AMBs of joint 2, (g'_{l1_2}, g'_{l3_2}, g'_{r1_2} and g'_{r3_2}) then, equation (34) can be solved, for joint 2, to obtain y_2, z_2, θ_2 and ψ_2.

The rotation matrix of frame f_3 w.r.t. frame f_2, ${}^2R_3$ is obtained from the following equation

$$ {}^2R_3 = R_{z,\psi_2} \times R_{y,\theta_2} \times R_{x,\phi_2} \tag{38} $$

$$ {}^2R_3 = \left[\begin{array}{ccc} c_{\psi_2} c_{\theta_2} & c_{\psi_2} s_{\phi_2} s_{\theta_2} - c_{\phi_2} s_{\psi_2} & s_{\phi_2} s_{\psi_2} + c_{\phi_2} c_{\psi_2} s_{\theta_2} \\ c_{\theta_2} s_{\psi_2} & c_{\phi_2} c_{\psi_2} + s_{\phi_2} s_{\psi_2} s_{\theta_2} & c_{\phi_2} s_{\psi_2} s_{\theta_2} - c_{\psi_2} s_{\phi_2} \\ -s_{\theta_2} & c_{\theta_2} s_{\phi_2} & c_{\phi_2} c_{\theta_2} \end{array}\right] \tag{39} $$

Then, the relation between frames f_2 and f_3 is determined from the following matrix

$$ {}^2H_3 = \left[\begin{array}{ccc|c} c_{\psi_2} c_{\theta_2} & c_{\psi_2} s_{\phi_2} s_{\theta_2} - c_{\phi_2} s_{\psi_2} & s_{\phi_2} s_{\psi_2} + c_{\phi_2} c_{\psi_2} s_{\theta_2} & g'_{la_2} \\ c_{\theta_2} s_{\psi_2} & c_{\phi_2} c_{\psi_2} + s_{\phi_2} s_{\psi_2} s_{\theta_2} & c_{\phi_2} s_{\psi_2} s_{\theta_2} - c_{\psi_2} s_{\phi_2} & y_2 \\ -s_{\theta_2} & c_{\theta_2} s_{\phi_2} & c_{\phi_2} c_{\theta_2} & z_2 \\ \hline 0 & 0 & 0 & 1 \end{array}\right] \tag{40} $$

where g'_{la_2} is the air gap deviation in the axial direction of joint 2. Thus, the relation between frames f_2 and f_4 is determined from the following equation

$$ {}^2H_4 = {}^2H_3 \times {}^3H_4 \tag{41} $$

Also, the relation between frames f_1 and f_2 is determined from the following matrix

$$ {}^1H_2 = \left[\begin{array}{ccc|c} 1 & 0 & 0 & {}^1x_2 \\ 0 & 1 & 0 & {}^1y_2 \\ 0 & 0 & 1 & {}^1z_2 \\ \hline 0 & 0 & 0 & 1 \end{array}\right] \tag{42} $$

where ${}^1x_2$, ${}^1y_2$, and ${}^1z_2$ are constants lengths.

The relation between frames f_0 and f_1 is determined as follows:

Knowing the air gap deviations of the radial AMBs of joint 1, (g'_{l1_1}, g'_{l3_1}, g'_{r1_1} and g'_{r3_1}) then, equation (34) can be solved, for joint 1, to obtain y_1, z_1, θ_1 and ψ_1.

The rotation matrix of frame f_1 w.r.t. frame f_0, ${}^0R_1$ is obtained from the following equation

$$ {}^0R_1 = R_{z,\psi_1} \times R_{y,\theta_1} \times R_{x,\phi_1} \tag{43} $$

$$ {}^0R_1 = \left[\begin{array}{ccc} c_{\psi_1} c_{\theta_1} & c_{\psi_1} s_{\phi_1} s_{\theta_1} - c_{\phi_1} s_{\psi_1} & s_{\phi_1} s_{\psi_1} + c_{\phi_1} c_{\psi_1} s_{\theta_1} \\ c_{\theta_1} s_{\psi_1} & c_{\phi_1} c_{\psi_1} + s_{\phi_1} s_{\psi_1} s_{\theta_1} & c_{\phi_1} s_{\psi_1} s_{\theta_1} - c_{\psi_1} s_{\phi_1} \\ -s_{\theta_1} & c_{\theta_1} s_{\phi_1} & c_{\phi_1} c_{\theta_1} \end{array}\right] \tag{44} $$

Then, the relation between frames f_0 and f_1 is determined from the following matrix

$$ {}^0H_1 = \left[\begin{array}{ccc|c} c_{\psi_1} c_{\theta_1} & c_{\psi_1} s_{\phi_1} s_{\theta_1} - c_{\phi_1} s_{\psi_1} & s_{\phi_1} s_{\psi_1} + c_{\phi_1} c_{\psi_1} s_{\theta_1} & g'_{la_1} \\ c_{\theta_1} s_{\psi_1} & c_{\phi_1} c_{\psi_1} + s_{\phi_1} s_{\psi_1} s_{\theta_1} & c_{\phi_1} s_{\psi_1} s_{\theta_1} - c_{\psi_1} s_{\phi_1} & y_1 \\ -s_{\theta_1} & c_{\theta_1} s_{\phi_1} & c_{\phi_1} c_{\theta_1} & z_1 \\ \hline 0 & 0 & 0 & 1 \end{array}\right] \tag{45} $$

where g'_{la_1} is the air gap deviation in the axial direction of joint 1. The relation between frames f_0 and f_2 is determined from the following equation

$$ {}^0H_2 = {}^0H_1 \times {}^1H_2 \tag{46} $$

Finally, using equations (41) and (46), the relation between frames f_0 and f_4 is determined from the following equation

$$ {}^0H_4 = {}^0H_2 \times {}^2H_4 \tag{47} $$

Thus, if the sensors data of the roll angle and the air gap deviations of the AMBs for each joint of the manipulator are given, then the end effector position and orientation can be obtained using forward kinematics equations.

Inverse kinematics

If the end effector has to move for a certain task, then its target position and orientation (x_e, y_e, z_e, ϕ_e, θ_e, ψ_e are known. Then, ${}^0H_4$ can be determined from the following equation

$$ {}^0H_4 = \left[\begin{array}{ccc|c} c_{\psi_e} c_{\theta_e} & c_{\psi_e} s_{\phi_e} s_{\theta_e} - c_{\phi_e} s_{\psi_e} & s_{\phi_e} s_{\psi_e} + c_{\phi_e} c_{\psi_e} s_{\theta_e} & x_e \\ c_{\theta_e} s_{\psi_e} & c_{\phi_e} c_{\psi_e} + s_{\phi_e} s_{\psi_e} s_{\theta_e} & c_{\phi_e} s_{\psi_e} s_{\theta_e} - c_{\psi_e} s_{\phi_e} & y_e \\ -s_{\theta_e} & c_{\theta_e} s_{\phi_e} & c_{\phi_e} c_{\theta_e} & z_e \\ \hline 0 & 0 & 0 & 1 \end{array}\right] \tag{48} $$

Afterward, for a chosen $g'_{la_2}, y_2, z_2, \phi_2, \theta_2$, and ψ_2 of joint 2, one can get g'_{l1_2}, g'_{r1_2}, g'_{l3_2}, and g'_{r3_2} from equation (34) and the required joint roll angle and the air gap deviations of AMB of joint 2 are obtained. Then, equation (41) is used to obtain ${}^2H_4$. After that, using equation (47), ${}^0H_2$ is determined.

Then, from equation (46) we get ${}^0H_1$. Then, using equation (45), one can get $g'_{la_1}, y_1, z_1, \phi_1, \theta_1$, and ψ_1 of joint 1. Finally, from equation (34), we can get g'_{l1_1}, g'_{r1_1}, g'_{l3_1}, and g'_{r3_1}. Thus, the required joint roll angle and the air gap deviations of AMB of joint 1 are obtained.

Control design

Control objectives

In order to control the end effector position, each joint roll angle is controlled using a PID-based feedback linearization method. In addition, the air gap lengths of the AMBs in the horizontal, vertical, and axial directions are controlled to be at the desired values using a state feedback controller with integral term.

PID-based feedback linearization

For the PID-based feedback linearization controller,[24] equations (19) and (20) are used to get the following control input that cancels out the nonlinearities

$$ T_e = \left(J_m + ML_a^2 \frac{P}{2}\right) U_\phi + MgL_a \cos(\phi) + b_f \omega_m \tag{49} $$

$$ U_\phi = \ddot{\phi}_d + K_p e + K_d \dot{e} + K_i \int_0^t e \, \mathrm{d}t \tag{50} $$

where ϕ_d is the desired robot joint angle and K_p, K_i, and K_d are the controller parameters.

The integral term is added to ensure robustness of the controller for payload variation. The objective of the controller is to minimize the error, $e = \phi_d - \phi$. In addition, the three-phase currents errors are controlled using P controller.[20]

State feedback controller

The five air gap deviations of the two radial AMBs, of each joint, in radial and axial directions are controlled using state feedback controllers with integral term. The optimal state feedback gains are calculated by knowing all the states of the system using Linear-Quadratic Regulator (LQR).[25]

In particular, for a certain required position and orientation of the end effector, the controllers obtain the actual air gap lengths of the 5-DOF AMBs and the actual roll angle from the sensors of each joint. Then, the controllers minimize the error between these values and the desired ones to achieve the required pose of the end effector.

Table 5. Joint 2 AMB parameters.

Parameter	Value	Parameter	Value
M	5 Kg	J_x	0.021 Kg·m^2
J_y	0.054 Kg·m^2	l	0.0685 m
$I_{l1,r1}$	0.7006 A	$I_{l2..l4,r2..l4}$	0.2577 A
D_o	1 mm	β	1066 N/m
γ_a	0.403 N·S/m		

AMB: active magnetic bearing.

Table 6. Joint 1 AMB parameters.

Parameter	Value	Parameter	Value
M	39.8 Kg	J_x	0.391 Kg·m^2
J_y	0.967 Kg·m^2	l	0.1405 m
$I_{l1,r1}$	1.858 A	$I_{l2..l4,r2..l4}$	0.2577 A
D_o	1 mm	β	1066 N/m
γ_a	0.403 N·S/m		

AMB: active magnetic bearing.

Stability analysis

To simplify the analysis, let us study the stability of linearized 1-DOF axial motion, given in "Axial motion" section in Appendix 2. Using Routh Hurwitz stability criterion,[26] the necessary and sufficient conditions for stability are

$$3.2e14\,K_I > 0 \tag{51}$$

$$3.5\,K_3 + 38.0 > 0 \tag{52}$$

$$K_A - \frac{3.2e14\,K_1 + 7.6e16\,K_3 + 8.1e17}{3.5\,K_3 + 38.0} > 0 \tag{53}$$

$$K_B - \frac{1.4e24\,K_I(7.0\,K_3 + 76.0)^2}{2.1e26\,K_2 - 5.5e24\,K_1 - 1.7e25\,K_3 + K_C} > 0 \tag{54}$$

where

$$K_A = 3.2e14\,K_2 + 0.57\,K_3 + 2.2e16 \tag{55}$$

$$K_B = 3.2e14\,K_1 + 7.6e16\,K_3 + 8.1e17 \tag{56}$$

$$K_C = 3.4e10\,K_3^2 + 1.9e25\,K_2\,K_3 + 4.5e26 \tag{57}$$

Moreover, equations (53) and (54) are solved using the method explained in Al-Salem et al.[27] to obtain K_1 and K_2.

From the above equations, and as a result, we found that the stability is guaranteed when the following conditions are satisfied

$$K_2 > 0 \tag{58}$$

$$K_3 > \frac{-38.0}{3.5} \tag{59}$$

$$K_I > 0 \tag{60}$$

where K_1, K_2, and K_3 are the state feedback controller gains and K_I is the integral term gain.

Simulation study

System finite element analysis

A study of the system is carried by CATIA design software using radial AMBs for joint 2 and joint 1 whose parameters are given in Tables 5 and 6 in respective order. This study is developed at the case where a robot arm is in a vertical position and at the worst loading condition when the robot arm is at a horizontal position. The system is studied under its weight effect as a result of the low speed of the robot joint.

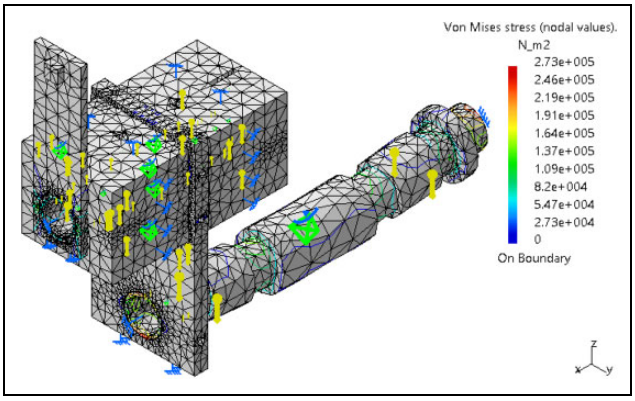

Figure 15. System stress analysis at vertical position.

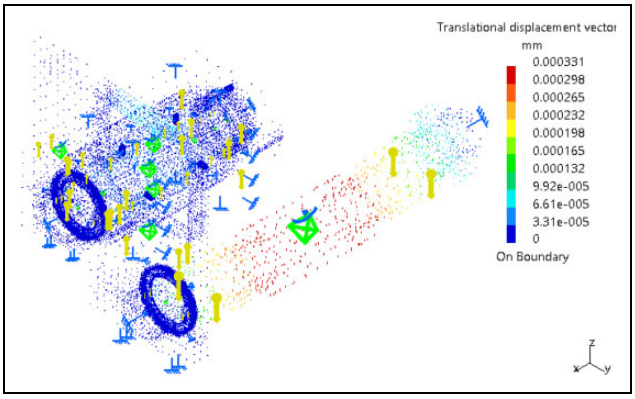

Figure 16. System deformation analysis at vertical position.

Figure 15 shows the stress analysis of the system for a vertical position robot arm, and the maximum stress is 0.273 MPa. Figure 16 shows the deformation analysis of the system in the same case, and the maximum deformation is 0.331 . Figure 17 shows the stress analysis of the system at worst case, and the maximum stress is 0.557 MPa. Figure 18 shows the deformation analysis of the system in the same case, and the maximum deformation is 1.2 μm.

The above finite element study proves that the obtained value of stress is safe compared with the allowable stress

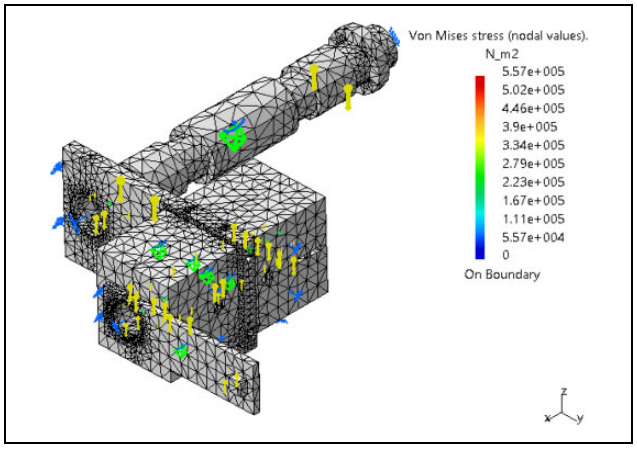

Figure 17. System stress analysis at horizontal position.

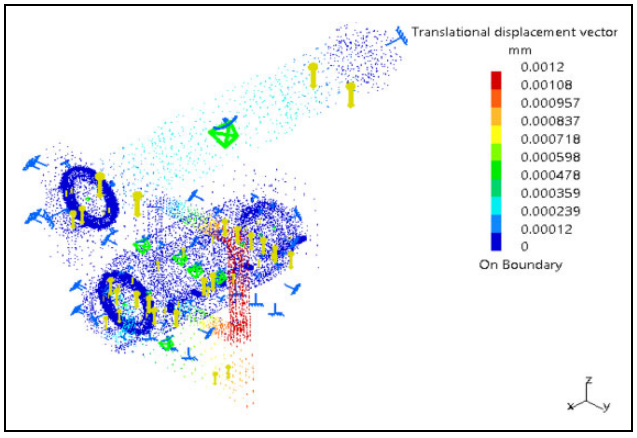

Figure 18. System deformation analysis at horizontal position.

Table 7. Joint 2 BLDC motor parameters.

Parameter	Value
Rated speed, n_{m2}	1500 r/min
Rated torque, T_{e2}	8 Nm
Phase resistance, R_2	7.9 Ω
Phase inductance, L_2	25.8 mH
Poles number, P_2	12
Back EMF constant, K_{p2}	3.13 V·S/rad
Inertia, J_{m2}	0.0008 Kg·m^2

BLDC: brushless DC.

value of steel, and the obtained value of displacement is much less than the air gap length which is 1 mm.

System simulation analysis

The BLDC motor parameters are given in Table 7 for joint 2 and Table 8 for joint 1. The system and its controllers represented by equations (14) to (50) are all simulated using MATLAB/Simulink.[28]

In order to control the end effector position and orientation of the proposed two-link manipulator to be, for example, at $(x_e, y_e, z_e) = (-250\ \mu m, 100\ \mu m, -150\ \mu m)$ and $(\phi_e, \theta_e, \psi_e) = (30^\circ, -125^{\mu\circ}, -225^{\mu\circ})$, considering macro positioning of the joint roll angle, $\phi_e = 30^\circ$, equation (34) and equation (37) to equation (48) are used to obtain the required robot joint roll angles (ϕ_2) and the air gap deviations of the radial and axial motions ($g'_{l1_2}, g'_{r1_2}, g'_{l3_2}, g'_{r3_2}, g'_{la_2}$) of joint 2 as well as (ϕ_1) and ($g'_{l1_1}, g'_{r1_1}, g'_{l3_1}, g'_{r3_1}, g'_{la_1}$) of joint 1.

Table 8. Joint 1 BLDC motor parameters.

Parameter	Value
Rated speed, n_{m1}	500 r/min
Rated torque, T_{e1}	67.6 Nm
Phase resistance, R_1	3.46 Ω
Phase inductance, L_1	28.2 mH
Back EMF constant, K_{p1}	4.78 V·S/rad
Inertia, J_{m1}	0.00319 Kg·m^2

BLDC: brushless DC.

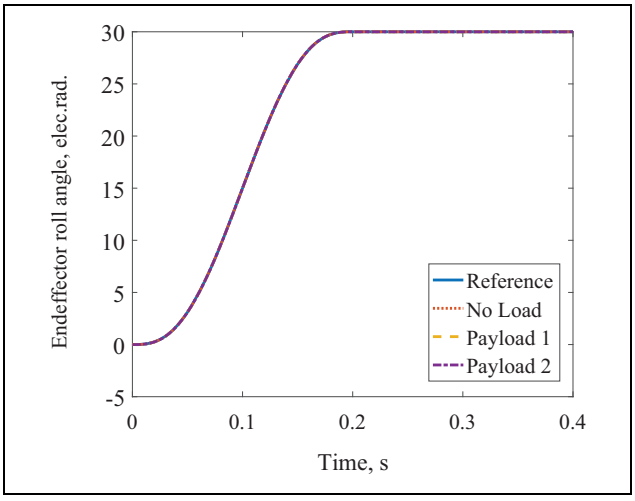

Figure 19. End effector roll angle, ϕ_e.

Thus, for the above required position and orientation of the end effector, ($g'_{l1_2}, g'_{r1_2}, g'_{l3_2}, g'_{r3_2}, g'_{la_2}, \phi_2$), of joint 2, are found to be $= (-149.79\ \mu m, -150.16\ \mu m, -99.64\ \mu m, -100.31\ \mu m, -250\ \mu m, 30^\circ)$ and ($g'_{l1_1}, g'_{r1_1}, g'_{l3_1}, g'_{r3_1}, g'_{la_1}, \phi_1$), of joint 1, are found to be $= (250\ \mu m, 250\ \mu m, 200\ \mu m, 200\ \mu m, 0\ \mu m, 0^\circ)$.

The controller then uses these obtained desired values of joint angles and the air gap deviations of the radial and axial motions to achieve the desired pose of the end effector. The results of the end effector position and orientation at no payload and for payload 1 of 0.1 kg and payload 2 of 0.2 kg are shown in Figures 19 to 24.

Results and discussion

It is noticed that the obtained figures show a slightly and acceptable change between the reference and actual values at the different values of payloads. Moreover, it is possible

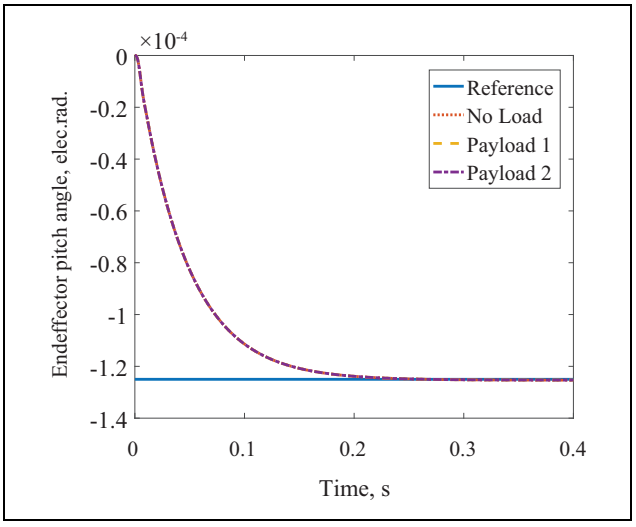

Figure 20. End effector pitch angle, θ_e.

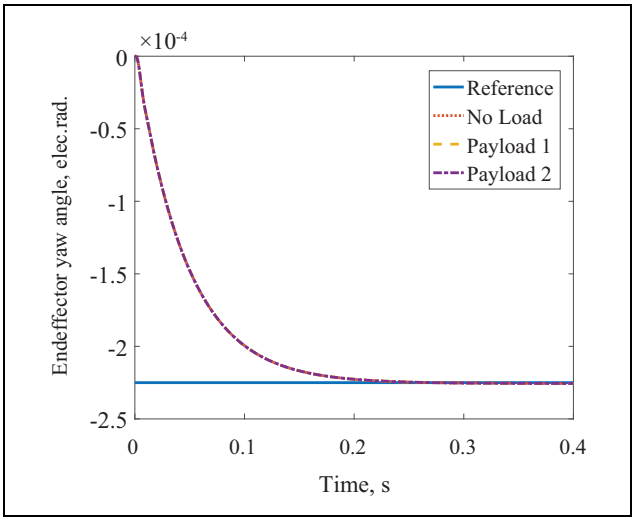

Figure 21. End effector yaw angle, ψ_e.

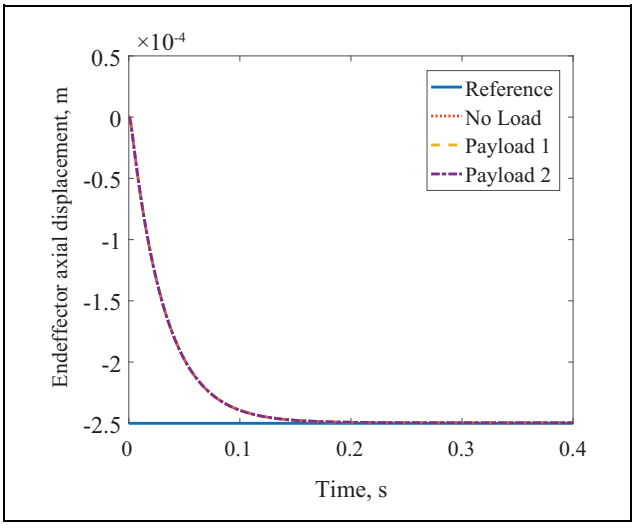

Figure 22. End effector axial motion, x_e.

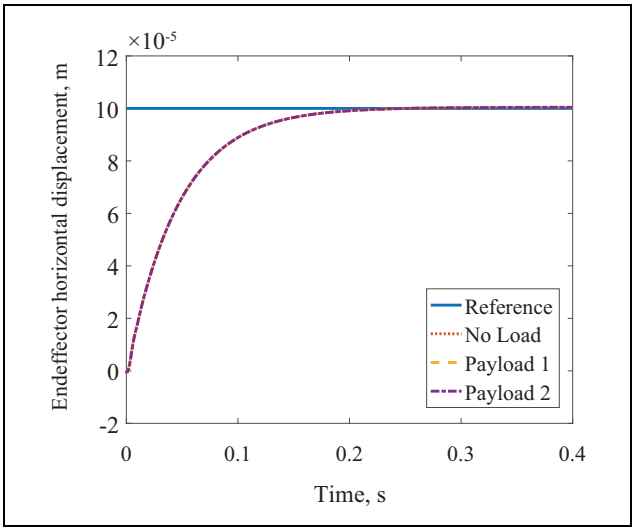

Figure 23. End effector horizontal motion, y_e.

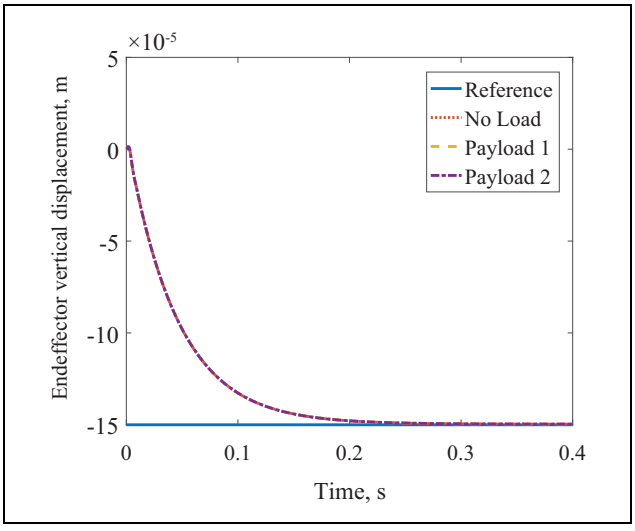

Figure 24. End effector vertical motion, z_e.

to recognize that the performance of the proposed manipulator is acceptable and the effectiveness of it in micromotion scale applications is achieved.

Conclusion

In this article, a two-link manipulator with two novel contactless 6-DOF joints is proposed. Description and design of the presented system are introduced. The radial and axial AMBs of each joint are designed in details. The stress and deflection of the system are calculated using FEA method and they are safe with respect to the maximum allowable steel stress and the air gap length. Mathematical modeling and system kinematics are carried out. For each joint, PID-based feedback linearization controller is designed to control the joint roll angle and a state feedback controller with an integral term is designed for controlling the AMB air

gap lengths. Stability of the controller is analyzed. The system with designed controllers has good performance and valid even if the payload is changed. Simulation results enlighten the feasibility of the proposed system and the efficiency of the end effector micromotion control. This proposed type of manipulator opens new application area for robotics. Such applications are clean and surgery rooms used in clean environments, self-reconfiguration robots, robots with selective compliance, industrial robots for laser cutting or arc welding, and space robots. As a future work, the proposed manipulator system will be tested experimentally.

Author's note

Mohamed Selmy on leave: Faculty of Engineering at Shoubra, Benha University, Banha, Egypt; Mohamed Fanni on leave: Prod. Eng. Mechanical Design Dept., Mansoura University, Mansoura, Egypt; and Abdelfatah M Mohamed on leave: Electrical Engineering Department, Faculty of Engineering, Asyut, Egypt.

Acknowledgments

The first author is supported by a scholarship from the Ministry of Higher Education, Government of Egypt which is gratefully acknowledged.

Declaration of conflicting interests

The author(s) declared no potential conflicts of interest with respect to the research, authorship, and/or publication of this article.

Funding

The author(s) received no financial support for the research, authorship, and/or publication of this article.

ORCID iD

Mohamed Selmy https://orcid.org/0000-0003-3180-8160

References

1. Higuchi T, Oka K, and Sugawara H. Clean room robot with non-contact joints using magnetic bearings. *Adv Robotics* 1993; 7(2): 105–119.
2. Darbandi SM, Behzad M, Salarieh H, et al. Linear output feedback control of a three-pole magnetic bearing. *IEEE/ASME Trans Mechatronics* 2014; 19(4): 1323–1330.
3. Schweitzer G, Bleuler H, Maslen E, et al. *Magnetic bearings: theory, design, and application to rotating machinery*. Berlin Heidelberg: Springer, 2009. ISBN 9783642004971. https://books.google.com.eg/books?id=1Kyg5dWyBasC.
4. Li Y, Lei G, Sun Y, et al. Dynamics of magnetic suspension rotor system of turbo-expander. *Int J Appl Electrom* 2017; 54(1): 1–12.
5. Ren X, Le Y, Han B, et al. Loss optimization and thermal analysis of a heteropolar magnetic bearing for a vacuum turbo-molecular pump. *Int J Appl Electrom* 2017; 54(4): 673–690.
6. Tezuka T, Kurita N, and Ishikawa T. Design and simulation of a five degrees of freedom active control magnetic levitated motor. *IEEE Trans Magn* 2013; 49(5): 2257–2262.
7. Selmy M, Fanni M, and Mohamed AM. Novel contactless active robotic joint using AMB: design and control. In: *ASME 2015 international design engineering technical conferences and computers and information in engineering conference*, Boston, Massachusetts, USA, 2–5 August 2015, pp. V009T07A072–V009T07A072. American Society of Mechanical Engineers.
8. Selmy M, Fanni M, and Mohamed AM. Micro/macro-positioning control of a novel contactless active robotic joint using active magnetic bearing. In: *2017 IEEE international conference on industrial technology (ICIT)*, Toronto, Onatario, Canada, 22–25 March 2017, pp. 671–676. DOI: 10.1109/ICIT.2017.7915439.
9. Higuchi M, Kawamura T, Kaikogi T, et al. (Mitsubishi clean room robot) Clean material handling originated from plant equipment inspection. *Mitsubishi Juko Giho* 2003; 40(5): 298–301.
10. Matsuda K and Kijimoto S. Reaction disturbance cancellation for a magnetically levitated ladder arm of clean-room robot. In: *IECON 2010-36th annual conference on IEEE industrial electronics society*, Glendale, Arizona, USA, 7–10 November 2010, pp. 1596–1602. IEEE
11. Mohammad AEK, Hong J, and Wang D. Design of a force-controlled end-effector with low-inertia effect for robotic polishing using macro-mini robot approach. *Robot Cim-Int Manuf* 2018; 49: 54–65. DOI: 10.1016/j.rcim.2017.05.011. http://www.sciencedirect.com/science/article/pii/S0736584516303647.
12. Božek P. Control of a robotic arm on the principle of separate decision of an inertial navigation system. *Appl Mech Mater* 2014; 611: 60–66. DOI: 10.4028/www.scientific.net/AMM.611.60.
13. Turygin Y, Bœk P, Nikitin Y, et al. Enhancing the reliability of mobile robots control process via reverse validation. *Int J Adv Robot Syst* 2016; 13(6): 1729881416680521. DOI: 10.1177/1729881416680521.
14. Lozhkin A, Abramov I, Nikitin Y, et al. The issue of calculating elliptic trajectories. *Manuf Technol* 2014; 14(4): 561–566.
15. Torque motor: frameless torque motors, direct drive motor—Alxion—torque motors, permanent magnet generators, resolvers, servo drives. http://www.alxion.com/products/stk-motors/ (accessed June 2018).
16. Carlson-Skalak S, Maslen E, and Teng Y. Magnetic bearing actuator design using genetic algorithms. *J Eng Design* 1999; 10(2): 143–164.
17. Jang SM, Lee UH, Choi JY, et al. Design and analysis of thrust active magnetic bearing. *J Appl Phys* 2008; 103(7): 07F122. DOI: 10.1063/1.2837649.
18. Barbaraci G. Axial active magnetic bearing design. *J Vib Control* 2016; 22(5): 1190–1197. DOI: 10.1177/1077546314534720.
19. 3D Modeling Solutions—CATIA—Dassault Systèmes®. https://www.3ds.com/products-services/catia/ (accessed June 2018).
20. Krishnan RR. *Permanent magnet synchronous and brushless DC motor drives*. Boca Raton; Abingdon: CRC Press; Taylor & Francis, 2010. ISBN 9780824753849.

21. Mohamed AM, Matsumura F, Namerikawa T, et al. Q-parameterization control of vibrations in a variable speed magnetic bearing. In: *Proceedings of the 1997 IEEE international conference on control applications, 1997*, Hartford, Connecticut, USA, 5–7 October 1997, pp. 540–546. IEEE.
22. Mohamed AM. *Optimal control design and nonlinear dynamics of magnetic bearing systems*. PhD Thesis, University of Maryland College Park, 1990.
23. Mohamed AM, Hassan IM, and Hashem AM. Application of discrete-time gain-scheduled q-parameterization controllers to magnetic bearing systems with imbalance. In: *Proceedings of the 1999 American control conference, 1999*, California, United States, 2–4 June 1999, volume 1. pp. 598–602. IEEE.
24. Slotine JJE and Li W. *Applied nonlinear control*. Upper Saddle River: Prentice-Hall, 1991.
25. Kwakernaak H and Sivan R. *Linear optimal control systems*. New York: Wiley-interscience, 1972, Vol 1.
26. Dorf RC and Bishop RH. *Modern control systems*. London, United Kingdom: Pearson, 1998.
27. Al-Salem N and Fanni M. Design of digital high-gain pd control systems using analytical approach. *JSME International Journal Series C Mechanical Systems Machine Elements Manufac* 2004; 47(3): 792–802.
28. MATLAB/Simulink—simulation and model based design. https://mathworks.com/products/simulink.html (accessed June 2018).

Appendix 1

State space representation of AMB

Radial motion. Considering the radial motion, equation (34) is rewritten as follow

$$g = c_{gz}\, z \tag{1A}$$

where

$$g = \begin{bmatrix} g'_{l1} \\ g'_{r1} \\ g'_{l3} \\ g'_{r3} \end{bmatrix} \tag{1B}$$

$$c_{gz} = \begin{bmatrix} 0 & 1 & -l & 0 \\ 0 & 1 & l & 0 \\ -1 & 0 & 0 & -l \\ -1 & 0 & 0 & l \end{bmatrix} \tag{1C}$$

$$z = \begin{bmatrix} y \\ z \\ \theta \\ \psi \end{bmatrix} \tag{1D}$$

Also

$$\ddot{g} = c_{gz}\, \ddot{z} \tag{1E}$$

Using equation (1E), equations (23) to (26) can be rewritten to be in the following form

$$\ddot{g} = \begin{bmatrix} \frac{-\omega_r J_x}{2J_y}(\dot{g}'_{l3} - \dot{g}'_{r3}) \\ \frac{\omega_r J_x}{2J_y}(\dot{g}'_{l3} - \dot{g}'_{r3}) \\ \frac{\omega_r J_x}{2J_y}(\dot{g}'_{l1} - \dot{g}'_{r1}) \\ \frac{-\omega_r J_x}{2J_y}(\dot{g}'_{l1} - \dot{g}'_{r1}) \end{bmatrix} + Df + DF_R \tag{1F}$$

where

$$D = \begin{bmatrix} -H_1 & H_2 & 0 & 0 \\ H_2 & -H_1 & 0 & 0 \\ 0 & 0 & -H_1 & H_2 \\ 0 & 0 & H_2 & -H_1 \end{bmatrix} \tag{1G}$$

$$H_1 = \frac{l^2}{J_y} + \frac{1}{m} \tag{1H}$$

$$H_2 = \frac{l^2}{J_y} - \frac{1}{m} \tag{1I}$$

$$f = \begin{bmatrix} f_{l1} - f_{l2} - \frac{1}{2}mg \\ f_{r1} - f_{r2} - \frac{1}{2}mg \\ f_{l3} - f_{l4} \\ f_{r3} - f_{r4} \end{bmatrix} \tag{1J}$$

$$F_R = \begin{bmatrix} f_{LV} \\ f_{RV} \\ f_{LH} \\ f_{RH} \end{bmatrix} \tag{1K}$$

Let the inputs

$$u_j = e_j \tag{1L}$$

where $j = l_1, l_2, r_1, r_2, l_3, l_4, r_3, r_4$.

The system states are defined as follows

$$x_1 = g'_{l1}, \quad x_2 = g'_{r1}, \quad x_3 = g'_{l3}, \quad x_4 = g'_{r3} \tag{1M}$$

$$x_5 = \dot{g}'_{l1}, \quad x_6 = \dot{g}'_{r1}, \quad x_7 = \dot{g}'_{l3}, \quad x_8 = \dot{g}'_{r3} \tag{1N}$$

$$\begin{aligned} &x_9 = i_{l1}, x_{10} = i_{l2}, x_{11} = i_{r1}, x_{12} = i_{r2}, \\ &x_{13} = i_{l3}, x_{14} = i_{l4}, x_{15} = i_{r3}, x_{16} = i_{r4} \end{aligned} \tag{1O}$$

Then, using equations (1F) and (27), the radial motion can be described by the following set of first order nonlinear differential equations

$$\dot{x}_1 = x_5, \quad \dot{x}_2 = x_6, \quad \dot{x}_3 = x_7, \quad \dot{x}_4 = x_8 \tag{1P}$$

$$\begin{aligned} \dot{x}_5 = {} & \frac{-\omega_r J_x}{2J_y}(x_7 - x_8) - H_1\left(f_{l1} - f_{l2} - \frac{1}{2}mg\right) \\ & + H_2\left(f_{r1} - f_{r2} - \frac{1}{2}mg\right) - H_1 f_{LV} + H_2 f_{RV} \end{aligned} \tag{1Q}$$

$$\dot{x}_6 = \frac{\omega_r J_x}{2J_y}(x_7 - x_8) + H_2\left(f_{l1} - f_{l2} - \frac{1}{2}mg\right) - H_1\left(f_{r1} - f_{r2} - \frac{1}{2}mg\right) + H_2 f_{LV} - H_1 f_{RV} \tag{1R}$$

$$\dot{x}_7 = \frac{\omega_r J_x}{2J_y}(x_5 - x_6) - H_1\left(f_{l3} - f_{l4} - \frac{1}{2}mg\right) + H_2\left(f_{r3} - f_{r4} - \frac{1}{2}mg\right) - H_1 f_{LH} + H_2 f_{RH} \tag{1S}$$

$$\dot{x}_8 = \frac{-\omega_r J_x}{2J_y}(x_5 - x_6) + H_2\left(f_{l3} - f_{l4} - \frac{1}{2}mg\right) - H_1\left(f_{r3} - f_{r4} - \frac{1}{2}mg\right) + H_2 f_{LH} - H_1 f_{RH} \tag{1T}$$

$$\dot{x}_9 = \frac{1}{L_C}(u_1 - R_C x_9) \tag{1U}$$

$$\dot{x}_{10} = \frac{1}{L_C}(u_2 - R_C x_{10}) \tag{1V}$$

$$\dot{x}_{11} = \frac{1}{L_C}(u_3 - R_C x_{11}) \tag{1W}$$

$$\dot{x}_{12} = \frac{1}{L_C}(u_4 - R_C x_{12}) \tag{1X}$$

$$\dot{x}_{13} = \frac{1}{L_C}(u_5 - R_C x_{13}) \tag{1Y}$$

$$\dot{x}_{14} = \frac{1}{L_C}(u_6 - R_C x_{14}) \tag{1Z}$$

$$\dot{x}_{15} = \frac{1}{L_C}(u_7 - R_C x_{15}) \tag{1a}$$

$$\dot{x}_{16} = \frac{1}{L_C}(u_8 - R_C x_{16}) \tag{1b}$$

The electromagnetic forces $f_{l1}, f_{l2}, f_{r1}, f_{r2}, f_{l3}, f_{l4}, f_{r3}, f_{r4}$ are expressed in terms of the states as follow

$$f_{l1} = K_2\left(\frac{x_9}{D_o + x_1}\right)^2\left(1 + \frac{2(D_o + x_1)}{\pi h}\right) \tag{1c}$$

$$f_{l2} = K_2\left(\frac{x_{10}}{D_o - x_1}\right)^2\left(1 + \frac{2(D_o - x_1)}{\pi h}\right) \tag{1d}$$

$$f_{r1} = K_2\left(\frac{x_{11}}{D_o + x_2}\right)^2\left(1 + \frac{2(D_o + x_2)}{\pi h}\right) \tag{1e}$$

$$f_{r2} = K_2\left(\frac{x_{12}}{D_o - x_2}\right)^2\left(1 + \frac{2(D_o - x_2)}{\pi h}\right) \tag{1f}$$

$$f_{l3} = K_2\left(\frac{x_{13}}{D_o + x_3}\right)^2\left(1 + \frac{2(D_o + x_3)}{\pi h}\right) \tag{1g}$$

$$f_{l4} = K_2\left(\frac{x_{14}}{D_o - x_3}\right)^2\left(1 + \frac{2(D_o - x_3)}{\pi h}\right) \tag{1h}$$

$$f_{r3} = K_2\left(\frac{x_{15}}{D_o + x_4}\right)^2\left(1 + \frac{2(D_o + x_4)}{\pi h}\right) \tag{1i}$$

$$f_{r4} = K_2\left(\frac{x_{16}}{D_o - x_4}\right)^2\left(1 + \frac{2(D_o - x_4)}{\pi h}\right) \tag{1j}$$

It can be seen from equations (1P) to (1j) that the 4-DOF radial motion is a MIMO system with 16 states, 8 inputs, and 4 outputs.

Axial motion. Considering the axial motion, equation (22) is represented in state variable form as follows: Let the inputs

$$u_j = e_j \tag{1k}$$

where $j = l_a, r_a$.

The system states are defined as follows

$$x_1 = g'_{la} \tag{1l}$$

$$x_2 = \dot{g}'_{la} \tag{1m}$$

$$x_3 = i_{la}, \quad x_4 = i_{ra} \tag{1n}$$

Then, using equations (22) and (27), the axial motion can be described by the following set of first order nonlinear differential equations

$$\dot{x}_1 = x_2 \tag{1o}$$

$$\dot{x}_2 = \frac{1}{m}(-2\gamma_a x_2 - \beta x_1 + f_{la} - f_{ra}) \tag{1p}$$

$$\dot{x}_3 = \frac{1}{L_C}(u_1 - R_C x_3) \tag{1q}$$

$$\dot{x}_4 = \frac{1}{L_C}(u_2 - R_C x_4) \tag{1r}$$

The electromagnetic forces f_{la}, f_{ra} are expressed in terms of the states as follows

$$f_{la} = K_2\left(\frac{x_3}{D_o + x_1}\right)^2\left(1 + \frac{2(D_o - x_1)}{\pi h}\right) \tag{1s}$$

$$f_{ra} = K_2\left(\frac{x_4}{D_o - x_1}\right)^2\left(1 + \frac{2(D_o - x_1)}{\pi h}\right) \tag{1t}$$

It can be seen from equations (1o) to (1t) that the 1-DOF axial motion is a multi input single output system with 4 states, 2 inputs and 1 output.

Appendix 2

AMB model linearization

The AMB nonlinear model is linearized at the equilibrium point using Jacobi matrix, Newton's method.

Radial motion. The following linearized model is obtained for the 4-DOF radial motion

$$\dot{x} = \boldsymbol{A_r}\, x + \boldsymbol{B_r}\, u \tag{2A}$$

Taking the air gap deviations as output variables, the output equation can be written as

$$y = \boldsymbol{C}_r\, x \tag{2B}$$

where

$$\boldsymbol{A_r} = \begin{bmatrix} \frac{\partial f_1}{\partial x_1} & \frac{\partial f_1}{\partial x_2} & \frac{\partial f_1}{\partial x_3} & \cdots & \frac{\partial f_1}{\partial x_{16}} \\ \frac{\partial f_2}{\partial x_1} & \frac{\partial f_2}{\partial x_2} & \frac{\partial f_2}{\partial x_3} & \cdots & \frac{\partial f_2}{\partial x_{16}} \\ \vdots & \vdots & \vdots & \ddots & \vdots \\ \frac{\partial f_{16}}{\partial x_1} & \frac{\partial f_{16}}{\partial x_2} & \frac{\partial f_{16}}{\partial x_3} & \cdots & \frac{\partial f_{16}}{\partial x_{16}} \end{bmatrix} \tag{2C}$$

where, $f_i = \dot{x}_i$, i = 1 to 16

$$\boldsymbol{B_r} = \begin{bmatrix} \frac{\partial f_1}{\partial u_1} & \frac{\partial f_1}{\partial u_2} & \frac{\partial f_1}{\partial u_3} & \cdots & \frac{\partial f_1}{\partial u_8} \\ \frac{\partial f_2}{\partial u_1} & \frac{\partial f_2}{\partial u_2} & \frac{\partial f_2}{\partial u_3} & \cdots & \frac{\partial f_2}{\partial u_8} \\ \vdots & \vdots & \vdots & \ddots & \vdots \\ \frac{\partial f_{16}}{\partial u_1} & \frac{\partial f_{16}}{\partial u_2} & \frac{\partial f_{16}}{\partial u_3} & \cdots & \frac{\partial f_{16}}{\partial u_8} \end{bmatrix} \tag{2D}$$

$$\boldsymbol{C_r} = [\,\mathbf{1_{4\times4}} \quad \mathbf{0_{4\times12}}] \tag{2E}$$

After linearization of the system at the equilibrium point, the final forms of matrices A and B are as follows

$$A_r = \begin{bmatrix} \mathbf{0_{4\times4}} & \mathbf{I_{4\times4}} & \mathbf{0_{4\times8}} \\ A\mathbf{1_{4\times4}} & A\mathbf{2_{4\times4}} & A\mathbf{3_{4\times8}} \\ \mathbf{0_{8\times8}} & A\mathbf{4_{8\times4}} & A\mathbf{5_{8\times4}} \end{bmatrix} \tag{2F}$$

$$\boldsymbol{B_r} = \frac{1}{L_C} \begin{bmatrix} 0 & \mathbf{0_{1\times4}} & \mathbf{0_{1\times3}} \\ 1 & \mathbf{0_{1\times4}} & \mathbf{0_{1\times3}} \\ 0 & 1 & \mathbf{0_{1\times6}} \\ \mathbf{0_{1\times2}} & 1 & \mathbf{0_{1\times5}} \\ \mathbf{0_{1\times3}} & 1 & \mathbf{0_{1\times4}} \\ \mathbf{0_{1\times4}} & 1 & \mathbf{0_{1\times3}} \\ \mathbf{0_{1\times5}} & 1 & \mathbf{0_{1\times2}} \\ \mathbf{0_{1\times6}} & 1 & 0 \\ \mathbf{0_{1\times6}} & 0 & 1 \end{bmatrix} \tag{2G}$$

where

$$A\mathbf{1_{4\times4}} = \begin{bmatrix} a_{(5,1)} & a_{(5,2)} & 0 & 0 \\ a_{(6,1)} & a_{(6,2)} & 0 & 0 \\ 0 & 0 & a_{(7,3)} & a_{(7,4)} \\ 0 & 0 & a_{(8,3)} & a_{(8,4)} \end{bmatrix} \tag{2H}$$

$$\mathbf{A2_{4\times4}} = \begin{bmatrix} 0 & 0 & a_{(5,7)} & a_{(5,8)} \\ 0 & 0 & a_{(6,7)} & a_{(6,8)} \\ a_{(7,5)} & a_{(7,6)} & 0 & 0 \\ a_{(8,5)} & a_{(8,6)} & 0 & 0 \end{bmatrix} \tag{2I}$$

$$A\mathbf{3_{4\times8}} = \begin{bmatrix} a_{(5,9)} & a_{(5,10)} & a_{(5,11)} & a_{(5,12)} & \mathbf{0_{1\times4}} \\ a_{(6,9)} & a_{(6,10)} & a_{(6,11)} & a_{(6,12)} & \mathbf{0_{1\times4}} \\ \mathbf{0_{1\times4}} & a_{(7,13)} & a_{(7,14)} & a_{(7,15)} & a_{(7,16)} \\ \mathbf{0_{1\times4}} & a_{(8,13)} & a_{(8,14)} & a_{(8,15)} & a_{(8,16)} \end{bmatrix} \tag{2J}$$

$$A\mathbf{4_{8\times4}} = \begin{bmatrix} \mathrm{diag}(a_{(9,9)}, a_{(10,10)}, a_{(11,11)}, a_{(12,12)}) \\ \mathbf{0_{4\times4}} \end{bmatrix} \tag{2K}$$

$$A\mathbf{5_{8\times4}} = \begin{bmatrix} \mathbf{0_{4\times4}} \\ \mathrm{diag}(a_{(13,13)}, a_{(14,14)}, a_{(15,15)}, a_{(16,16)}) \end{bmatrix} \tag{2L}$$

$$a_{(5,1)} = -c_1\left((c_3 - c_4 - c_5)\, x_9^2 - (-c_3 + c_4 + c_5)\, x_{10}^2\right) \tag{2M}$$

$$a_{(5,2)} = c_2\left((c_3 - c_4 - c_5)\, x_{11}^2 - (-c_3 + c_4 + c_5)\, x_{12}^2\right) \tag{2N}$$

$$a_{(5,7)} = \frac{-\omega_r J_x}{2J_y} \tag{2O}$$

$$a_{(5,8)} = \frac{\omega_r J_x}{2J_y} \tag{2P}$$

$$a_{(5,9)} = (-2c_6 - 4c_7)\, x_9 \tag{2Q}$$

$$a_{(5,10)} = (2c_6 + 4c_7)\, x_{10} \tag{2R}$$

$$a_{(5,11)} = (2c_8 + 4c_9)\, x_{11} \tag{2S}$$

$$a_{(5,12)} = (-2c_8 - 4c_9)\, x_{12} \tag{2T}$$

$$a_{(6,1)} = c_2\left((c_3 - c_4 - c_5)\, x_9^2 - (-c_3 + c_4 + c_5)\, x_{10}^2\right) \tag{2U}$$

$$a_{(6,2)} = -c_1\left((c_3 - c_4 - c_5)\, x_{11}^2 - (-c_3 + c_4 + c_5)\, x_{12}^2\right) \tag{2V}$$

$$a_{(6,7)} = \frac{\omega_r J_x}{2J_y} \tag{2W}$$

$$a_{(6,8)} = \frac{-\omega_r J_x}{2J_y} \tag{2X}$$

$$a_{(6,9)} = (2c_8 + 4c_9)\, x_9 \tag{2Y}$$

$$a_{(6,10)} = (-2c_8 - 4c_9)\, x_{10} \tag{2Z}$$

$$a_{(6,11)} = (-2c_6 - 4c_7)\, x_{11} \tag{2a}$$

$$a_{(6,12)} = (2c_6 + 4c_7)\, x_{12} \tag{2b}$$

$$a_{(7,3)} = -c_1\left((c_3 - c_4 - c_5)\, x_{13}^2 - (-c_3 + c_4 + c_5)\, x_{14}^2\right) \tag{2c}$$

$$a_{(7,4)} = c_2\left((c_3 - c_4 - c_5)\, x_{15}^2 - (-c_3 + c_4 + c_5)\, x_{16}^2\right) \tag{2d}$$

$$a_{(7,5)} = \frac{\omega_r J_x}{2J_y} \tag{2e}$$

$$a_{(7,6)} = \frac{-\omega_r J_x}{2J_y} \tag{2f}$$

$$a_{(7,13)} = (-2c_6 - 4c_7)\, x_{13} \tag{2g}$$

$$a_{(7,14)} = (2c_6 + 4c_7)\, x14 \tag{2h}$$

$$a_{(7,15)} = (2c_8 + 4c_9)\, x15 \tag{2i}$$

$$a_{(7,16)} = (-2c_8 - 4c_9)\, x16 \tag{2j}$$

$$a_{(8,3)} = c_2\left((c_3 - c_4 - c_5)\, x_{13}^2 - (-c_3 + c_4 + c_5)\, x_{14}^2\right) \tag{2k}$$

$$a_{(8,4)} = -c_1\left((c_3 - c_4 - c_5)\, x_{15}^2 - (-c_3 + c_4 + c_5)\, x_{16}^2\right) \tag{2l}$$

$$a_{(8,5)} = \frac{-\omega_r J_x}{2J_y} \tag{2m}$$

$$a_{(8,6)} = \frac{\omega_r J_x}{2J_y} \tag{2n}$$

$$a_{(8,13)} = (2c_8 + 4c_9)\, x_{13} \tag{2o}$$

$$a_{(8,14)} = (-2c_8 - 4c_9)\, x_{14} \tag{2p}$$

$$a_{(8,15)} = (-2c_6 - 4c_7)\, x_{15} \tag{2q}$$

$$a_{(8,16)} = (2c_6 + 4c_7)\, x_{16} \tag{2r}$$

$$a_{(9,9)} = \frac{-R_C}{L_C} \tag{2s}$$

$$a_{(9,9)} = a_{(10,10)} = a_{(11,11)} = a_{(12,12)} = a_{(13,13)} = a_{(14,14)} = a_{(15,15)} = a_{(16,16)} \tag{2t}$$

$$c_1 = H_1 K_2 \tag{2u}$$

$$c_2 = H_2 K_2 \tag{2v}$$

$$c_3 = \frac{2}{\pi h D_o} \tag{2w}$$

$$c_4 = \frac{2}{D_o^3} \tag{2x}$$

$$c_5 = \frac{4}{\pi h D_o^2} \tag{2y}$$

$$c_6 = \frac{c_1}{D_o^2} \tag{2z}$$

$$c_7 = \frac{c_1}{\pi h D_o} \tag{2A′}$$

$$c_8 = \frac{c_2}{D_o^2} \tag{2B′}$$

$$c_9 = \frac{c_2}{\pi h D_o} \tag{2C′}$$

Axial motion. The following linearized model is obtained for the 1-DOF axial motion:

$$\dot{x} = \boldsymbol{A_a}\, x + \boldsymbol{B_a}\, u \tag{2D′}$$

Taking the axial air gap deviation as output variable, the output equation can be written as:

$$y = \boldsymbol{C_a}\, x \tag{2E′}$$

where

$$\boldsymbol{A_a} = \begin{bmatrix} \frac{\partial f_1}{\partial x_1} & \frac{\partial f_1}{\partial x_2} & \frac{\partial f_1}{\partial x_3} & \frac{\partial f_1}{\partial x_4} \\ \frac{\partial f_2}{\partial x_1} & \frac{\partial f_2}{\partial x_2} & \frac{\partial f_2}{\partial x_3} & \frac{\partial f_2}{\partial x_4} \\ \frac{\partial f_3}{\partial x_1} & \frac{\partial f_3}{\partial x_2} & \frac{\partial f_3}{\partial x_3} & \frac{\partial f_3}{\partial x_4} \\ \frac{\partial f_4}{\partial x_1} & \frac{\partial f_4}{\partial x_2} & \frac{\partial f_4}{\partial x_3} & \frac{\partial f_4}{\partial x_4} \end{bmatrix} \tag{2F′}$$

where, $f_i = \dot{x}_i$, i = 1 to 4

$$\boldsymbol{B_a} = \begin{bmatrix} \frac{\partial f_1}{\partial u_1} & \frac{\partial f_1}{\partial u_2} \\ \frac{\partial f_2}{\partial u_1} & \frac{\partial f_2}{\partial u_2} \\ \frac{\partial f_3}{\partial u_1} & \frac{\partial f_3}{\partial u_2} \\ \frac{\partial f_4}{\partial u_1} & \frac{\partial f_4}{\partial u_2} \end{bmatrix} \tag{2G′}$$

$$\boldsymbol{C_a} = [\mathbf{1_{1\times 3}} 0] \tag{2H′}$$

After linearization of the system at equilibrium point, the final forms of matrices A_a and B_a are as follows

$$\boldsymbol{A_a} = \begin{bmatrix} 0 & 0 & 1 & 0 \\ A_{(2,1)} & A_{(2,2)} & A_{(2,3)} & A_{(2,4)} \\ 0 & 0 & \frac{-R}{L_C} & 0 \\ 0 & 0 & 0 & \frac{-R}{L_C} \end{bmatrix} \tag{2I′}$$

$$\boldsymbol{B_a} = \frac{1}{L_C} \begin{bmatrix} 0 & 0 \\ 0 & 0 \\ 1 & 0 \\ 0 & 1 \end{bmatrix} \tag{2J′}$$

where

$$a_{(2,1)} = -\left(\beta + (2K2\,x4^2\,((2h\,(Do - x1))/\pi + 1))/(Do - x1)^3 + (2K2\,x3^2\,((2h\,(Do + x1))/\pi + 1))/(Do + x1)^3 - (2K2\,h\,x3^2)/(\pi\,(Do + x1)2^{)} - (2\,K2\,h\,x4^2)/(\pi\,(Do - x1)^2)\right)/m \quad (2K')$$

$$a_{(2,2)} = -(2\gamma_a)/m \quad (2L')$$

$$a_{(2,3)} = (2K2\,x3((2h\,(Do + x1))/\pi + 1))/(m\,(Do + x1)^2) \quad (2M')$$

$$a_{(2,4)} = -(2K2\,x4((2h\,(Do - x1))/\pi + 1))/(m\,(Do - x1)^2) \quad (2N')$$